

# Three-dimensional computational analysis of transport phenomena in a PEM fuel cell—a parametric study

T. Berning\*, N. Djilali

*Institute for Integrated Energy Systems, University of Victoria, Victoria, Canada*

Received 30 May 2003; accepted 12 June 2003

---

## Abstract

This paper presents the results of a parametric study conducted with a previously described three-dimensional, non-isothermal model of a polymer electrolyte membrane (PEM) fuel cell. The effect of various operational parameters such as the temperature and pressure on the fuel cell performance was investigated in detail. It was found that in order to obtain physically realistic results experimental measurements of various modelling parameters were needed. The results show good qualitative agreement with experimental results published in the literature. In addition, geometrical and material parameters such as the gas diffusion electrode (GDE) thickness and porosity as well as the ratio between the channel width and the land area were investigated. The contact resistance inside the cell was found to play an important role for the evaluation of the impact of such parameters on the fuel cell performance. The results demonstrate the usefulness of this computational model as a design and optimization tool.

© 2003 Elsevier B.V. All rights reserved.

**Keywords:** PEM fuel cells; Fuel cell modelling; Computational modelling; Parametric study; Contact resistance

---

## 1. Introduction

Fuel cells convert the chemical energy of hydrogen and oxygen directly into electricity. Their high efficiency and low emissions have made them a prime candidate for powering the next generation of electric vehicles, and their modular design and the prospects of micro-scaling them have gained the attention of cellular phone and laptop manufacturers. Their scalability makes them prime candidates for a variety of stationary applications including distributed residential power generation. The basic structure and operation principle the polymer electrolyte membrane (PEM) fuel cell considered here are illustrated in Fig. 1.

The polymer electrolyte consists of a perfluorinated polymer backbone with sulfonic acid side chains. When fully humidified, this material becomes an excellent protonic conductor. The membrane and the two electrodes (teflonated porous carbon paper or cloth with platinum on supported carbon) are assembled into a sandwich structure to form a membrane-electrode assembly (MEA). The MEA is placed between two graphite bipolar plates with machined grooves

that provide flow channels for distributing the fuel (hydrogen) and oxidant (oxygen from air).

The hydrogen-rich fuel is fed to the anode, where the hydrogen diffuses through the porous gas diffusion electrode (GDE). At the catalyst layer, the hydrogen splits into hydrogen protons and electrons according to:



Driven by an electric field, the  $\text{H}^+$  ions migrate through the polymer electrolyte membrane. The oxygen in the cathode gas stream diffuses through the gas diffusion electrode towards the catalyst interface where it combines with the hydrogen protons and the electrons to form water according to:



The overall reaction is exothermic and can be written as:



Several coupled fluid flow, heat and mass transport processes occur in a fuel cell in conjunction with the electrochemical reaction. These processes have a significant impact on two important operational issues: (i) thermal and water management, and (ii) mass transport limitations. Water management ensures that the polymer electrolyte membrane remains fully hydrated to maintain good ionic conductivity

---

\* Corresponding author. Present address: Institute for Material Technology, Group of Electrochemistry, NTNU Trondheim, Norway.  
E-mail addresses: [torsten.berning@material.ntnu.no](mailto:torsten.berning@material.ntnu.no) (T. Berning), [ndjilali@uvic.ca](mailto:ndjilali@uvic.ca) (N. Djilali).

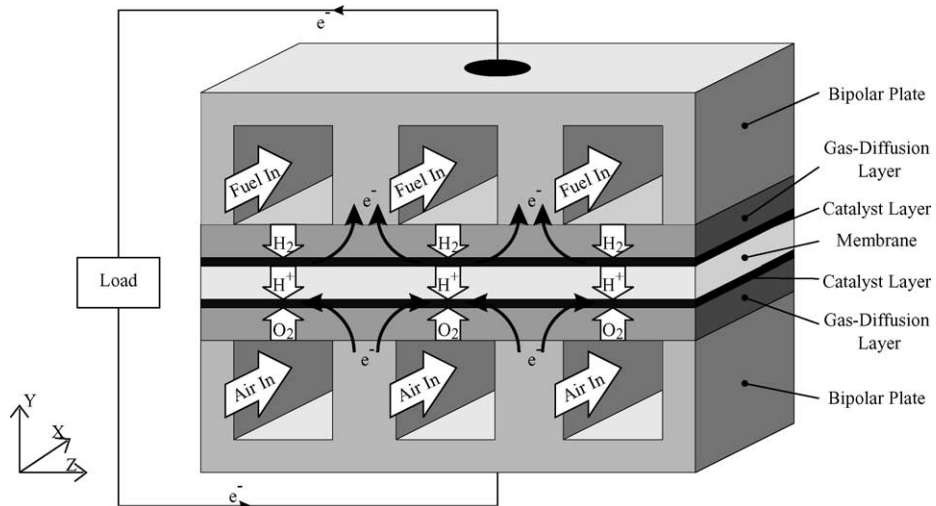


Fig. 1. Schematic of a PEM fuel cell.

and performance. Water content of the membrane is determined by the balance between water production and three water transport processes: electro-osmotic drag of water, associated with proton migration through the membrane from the anode to the cathode side; back diffusion from the cathode; and diffusion of water to/from the oxidant/fuel gas streams. Without control, an imbalance between production and removal rates of water can occur. This results in either dehydration of the membrane, or flooding of the electrodes; both phenomena have a very detrimental effect on performance and fuel cells have to be carefully designed to avoid the occurrence of either phenomenon. Thermal management is required to remove the heat produced by the electrochemical reaction in order to prevent drying out of the membrane and excessive thermal stresses that may result in rupture of the membrane. The small temperature differentials between the fuel cell stack and the operating environment make thermal management a challenging problem in PEMFC's.

Because of the highly reactive environment and compact nature of a fuel cell it is not possible to perform detailed *in situ* measurements during operation. Such information has been sought through modelling and simulation in order to improve understanding of water and species transport, optimize thermal management and shorten the design and optimization cycles. Modelling of fuel cells is challenging, because the processes involve multi-component, multi-phase, and multi-dimensional flow, heat and mass transfer with electrochemical reactions all occurring in irregular geometries including porous media. Numerous authors have developed fuel cell models accounting for various physical processes. The most prominent earlier works stem from Bernardi and Verbrugge [1,2] and Springer et al. [3], who developed one-dimensional, isothermal models of the membrane-electrode assembly. Fuller and Newman [4] published a quasi two-dimensional model based on concentration theory. The work by Nguyen and White [5], Yi and Nguyen [6] was two-dimensional in nature, but the

gas diffusion electrodes were omitted, assuming "ultrathin" electrodes. The importance of accounting for temperature gradients in fuel cells modelling was demonstrated in the work of Wöhr et al. [7] and Djilali and Lu [8]. The important issue of water flooding was addressed by Baschuk and Li in a one-dimensional model [9].

Earlier models were primarily analytic and required a number of simplifications due to the limitations of the numerical techniques. More recently, a general trend can be observed to apply the methods of computational fluid dynamics to fuel cell modelling. Gurau et al. [10] published a fully two-dimensional model of a whole fuel cell, i.e. two gas flow channels separated by the membrane-electrode assembly. Wang et al. [11,12] have developed a similar model and included two-phase flow.

In an earlier publication, our research group has presented a non-isothermal, three-dimensional model of a complete single cell [13]. Phase-change and multi-phase flow, however, could not be addressed with that model. Recently, Dutta et al. [14] published a three-dimensional computational model based on the commercial software package *Fluent*, which is quite similar to the one we presented earlier, except that it accounts for a partially dehydrated membrane using an empirical approach.

Overall, it can be said that whereas the focus of earlier modelling efforts was often one-dimensional with focus on the electrochemistry, more recent publications utilize the methods of computational fluid dynamics in order to devise multi-dimensional and multi-phase models.

## 2. Model description

A detailed description of the model has recently been published [13] and shall not be repeated here. In brief, the model is based on the commercial software package CFX-4.3 (AEA Technology) and considers single-phase, multi-component

flow inside the gas flow channels and the porous media. Water vapour is assumed to exist at its saturation pressure in both gas streams. The physical domain consists of a straight channel of 5 cm length and rectangular cross-section. Because of the symmetry assumption only half a channel and half a land area in between has to be modelled. For computational convenience the physical domain has been split up into four domains, allowing for conjugate heat transfer between the fluid-phase and the solid matrix of the porous medium in one domain, liquid water flux through the membrane and the GDE in a second subdomain and the electrical field in the membrane in the fourth domain with appropriate boundary conditions.

Overall, the model solves for the multi-component flow in the channels and the porous media with heat transfer. In addition, several phenomenological equations are implemented in a suite of user-subroutines, which are:

- the generalized Fick's law for multi-component diffusion [15];
- the Butler–Volmer equation for reaction kinetics [16];
- the Nernst–Planck equation for the transport of protons through the membrane [16]; and
- a modified version of the Schlögl equation to account for the flux of liquid water through the membrane [17].

The cell voltage is calculated at the end of each computation, accounting for the various loss mechanisms, according to:

$$E = E_{T,p}^0 - \eta_{\text{act}} - \eta_{\text{contact}} - \eta_{\text{mem}} \quad (4)$$

where the reversible cell potential  $E_{T,p}^0$  is being calculated as function of the temperature and pressure using the Nernst equation, and the activation overpotential  $\eta_{\text{act}}$  is calculated employing the Tafel equation by assuming an apparent exchange current density that depends on parameters such as the operation temperature, pressure and the catalyst loading. In contrast to [13] in the current paper the ohmic loss also includes a loss due to contact resistance at the interface between the bipolar plates and the gas diffusion layers, which have so far been neglected in virtually all modelling studies. The voltage loss due to contact resistance can be assumed of ohmic nature, i.e.

$$\eta_{\text{contact}} = ir_{\text{contact}} \quad (5)$$

where  $r_{\text{contact}}$  is an assumed contact resistance in ( $\Omega \text{cm}^2$ ) that varies with the porosity of the gas diffusion layer and the contact area between the bipolar plates and the gas diffusion layer, i.e. the ratio between the channel width and the land area. This will be explained in detail, later. The membrane loss  $\eta_{\text{mem}}$  is calculated assuming the membrane is fully hydrated at all times so that the protonic conductivity remains constant.

The basic capabilities and limitations of the current model have been outlined in detail in an earlier publication [13]. The current paper focuses on a parametric study

conducted with this model in order to assess the impact of the various fuel cell operating and material parameters on the fuel cell performance. In the following section only the parameter investigated is changed, all other parameters are at the base case conditions as outlined in [13].

### 3. Results and discussion

#### 3.1. Effect of temperature

In order to successfully model the effect of the temperature on the fuel cell performance, a basic understanding of its *direct* influence on various model parameters is required. The properties most dependent on temperature are as following.

- The *composition of the incoming gas streams*. Assuming the inlet gases are fully humidified, the partial pressure of water vapour entering the cell depends on the temperature only. Thus, the molar fraction of water vapour is a function of the inlet pressure and temperature, and so the molar fraction of the incoming hydrogen and oxygen depend on the temperature and pressure as well.
- The *exchange current density*  $i_0$  of the oxygen reduction reaction (ORR) increases rapidly with temperature due to the enhanced reaction kinetics. Parthasarathy et al. [18] conducted experiments in order to determine a correlation between the cell temperature and the exchange current density of the oxygen reduction reaction.
- The *membrane conductivity*  $\kappa$  increases, because a higher temperature leads also to a higher diffusivity of the hydrogen protons in the electrolyte membrane, thereby reducing the membrane resistance [1].
- The *reference potential*  $E^0$ . Although the Nernst equation [16] shows a decrease in the reference potential with an increasing temperature, experimental results indicate an increase, which can be explained with a higher diffusivity of the hydrogen with increasing temperature [18].
- The *gas-pair diffusivities*  $D_{ij}$  in the Stefan–Maxwell equations. An increase in temperature leads to an increase in the binary gas-pair diffusivities [19].

In order to determine the inlet gas composition as a function of temperature, the following relation between the temperature and the saturation pressure of water has been used [3]:

$$\log_{10} p_{\text{sat}} = -2.1794 + 0.02953 \times \vartheta - 9.1837E - 5 \times \vartheta^2 + 1.4454E - 7 \times \vartheta^3 \quad (6)$$

where  $\vartheta$  is the temperature ( $^{\circ}\text{C}$ ). The molar fraction of water vapour in the incoming gas stream is simply the ratio of the saturation pressure and the total pressure:

$$x_{\text{H}_2\text{O,in}} = \frac{p_{\text{sat}}}{p_{\text{in}}} \quad (7)$$

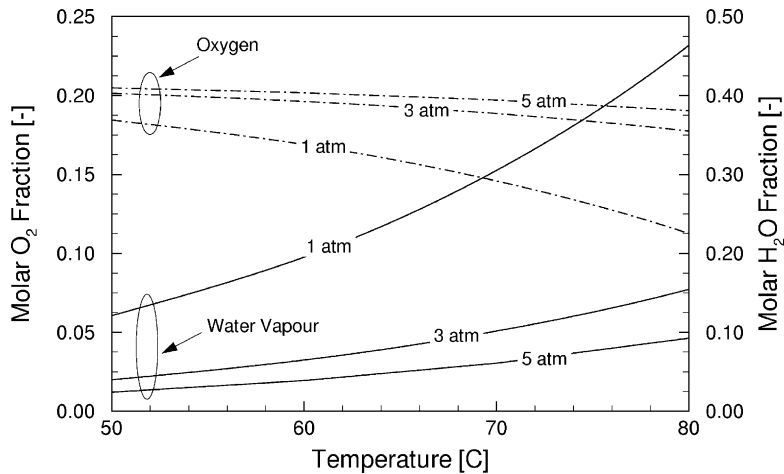


Fig. 2. Molar inlet composition of the cathode side gas stream as function of temperature.

Since the ratio of nitrogen and oxygen in dry air is known to be 79:21, the inlet oxygen fraction can be found via:

$$x_{O_2,\text{in}} = \frac{1 - x_{H_2O,\text{in}}}{1 + (79/21)} \quad (8)$$

The resulting inlet gas composition for different pressures is shown in Fig. 2. Clearly, at an operating pressure of 1 atm the effect of the temperature on the inlet composition is much stronger than at elevated pressures. At 80 °C for atmospheric pressure, almost 50% (molar) of the incoming cathode side gas stream consists of water vapour and only around 11% is oxygen.

In order to find a correlation between the reference exchange current density  $i_0$  for the oxygen reduction reaction at the cathode side and the temperature, experimental results obtained by Parthasarathy et al. [18] were used. The catalyst loading in those experiments did not correspond to the loading in our simulated cell. A method for estimating the variation of the exchange current density with temperature was devised (see [20]) and is used here. Table 1 shows the resulting exchange current densities used in our model for a range of temperatures. The exchange current density for a given catalyst loading varies by an order of magnitude from 323 to 353 K, and this is consistent with the results of Parthasarathy et al. [18]. Note that the base case temperature in this study was 353 K.

The conductivity of the electrolyte membrane is also a strong function of temperature. A theoretical expression derived by Bernardi and Verbrugge [2] shows that it depends

linearly on the diffusivity of the hydrogen proton inside the membrane  $D_{H^+}$ , which, in turn, was calculated according to [21]:

$$\frac{D_{H^+}\mu(T)}{T} = \text{const.} \quad (9)$$

where  $\mu(T)$  was taken by Bernardi and Verbrugge to be the viscosity of water. The resulting diffusivities for various temperatures are listed in the second column of Table 2, using the value of  $1.4 \times 10^{-5} \text{ cm}^2/\text{s}$  at 22 °C as measured by Verbrugge and Hill [22] as a benchmark. However, membrane conductivities computed using this approach do not match measured values. For the present simulation the membrane conductivity was taken to be  $6.8 \times 10^{-2} \text{ S/cm}$  at 80 °C [3], and a linear scaling with protonic diffusivity was used to estimate values at other temperatures.

The reversible cell potential  $E^0$  at various temperatures was computed using the Nernst equation:

$$E^0 = 1.23 - 0.9 \times 10^{-3}(T - 298) + 2.3 \frac{RT}{4F} p_{H_2}^2 p_{O_2} \quad (10)$$

Finally, the binary diffusivities of the gas-phase pairs had to be scaled with temperature. Different theoretical predictions of the binary diffusivity values can be found in the literature, and the one taken here was [19]:

$$D_{ij}(T) = D_{ij}(T_0) \left[ \frac{T}{T_0} \right]^{1.75} \quad (11)$$

The polarization curves obtained for various cell temperatures and using the above parameter values are shown in

Table 1

Apparent exchange current density of the ORR as a function of temperature

$T$ (K)	$i_0$ ( $\text{A}/\text{cm}^2$ )
323	$3.3 \times 10^{-8}$
333	$7.9 \times 10^{-7}$
343	$1.7 \times 10^{-7}$
353	$4.4 \times 10^{-7}$

Table 2

Proton diffusivity and membrane conductivity as function of temperature

$T$ (K)	$D_{H^+}$ ( $\text{cm}^2/\text{s}$ )	$\kappa$ ( $\text{S}/\text{cm}$ )
353	$4.54 \times 10^{-5}$	0.068
343	$3.87 \times 10^{-5}$	0.058
333	$3.26 \times 10^{-5}$	0.049
323	$2.75 \times 10^{-5}$	0.041

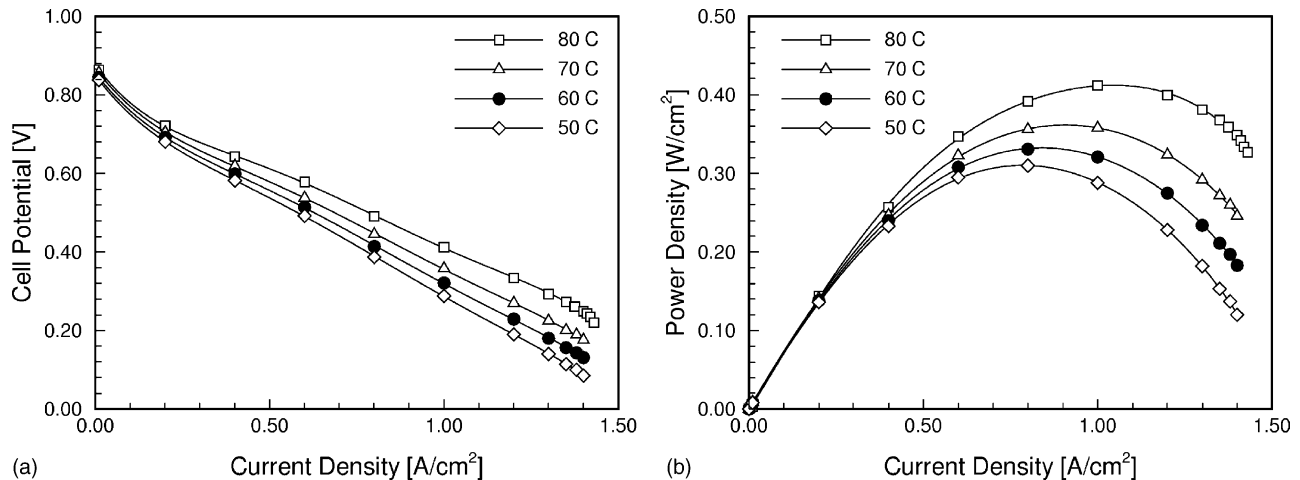


Fig. 3. Predicted polarization curves (a) and power density curves (b) for different cell temperatures. All other parameters are at base case conditions.

**Fig. 3.** The change in the initial drop due to the lower exchange current density is relatively small compared to the drop-off in the linear region, where ohmic losses are predominant. The limiting current density is very similar in all cases. This is due to the fact that the base case pressure is high (5 atm), and hence the inlet gas composition changes little with temperature (cf. Fig. 2). Changes in operating pressure on the other hand have a large impact on the inlet composition and, hence, on the limiting current density, as will be shown below. We note in Fig. 3 that the maximum power density shifts towards higher current density with an increasing temperature as a result of reduced ohmic losses [23].

A systematic comparison with experimental results is difficult, since the exact experimental conditions are frequently incompletely documented. As the current model has historically been developed as a three-dimensional version of the model by Bernardi and Verbrugge [2], who in turn matched their modelling data to experiments conducted by Ticianelli et al. [24], this shall be the first comparison made. Fig. 4

shows experimental results obtained for two different fuel cells and at different temperatures. Qualitatively, the results agree with our numerical data.

Kim et al. [25] extended the curve-fitting approach that was suggested by Ticianelli et al. in order to include the drop-off due to mass transport limitations at high current densities. The corrected equation is [25]:

$$E = E_r - b \log \frac{i}{i_0} - R_i i - m \exp(ni) \quad (12)$$

where  $E_r$  is the reversible cell potential for the given conditions and the three following terms describe the various loss mechanisms. The first term can be recognized as the Tafel equation that describes the activation overpotential, which is predominant at low current densities. The second term  $R_i$  describes a linear drop-off, which is predominant in the intermediate current density region, where  $R_i$  is the internal resistance caused by membrane and contact losses. The last term becomes predominant in the high current density region, and is used to match the drop-off towards the limiting current density. A physical interpretation for the parameters  $m$  and  $n$  was not given, but Bevers et al. [26] found in their one-dimensional modelling study that  $m$  correlates to the electrolyte conductivity and  $n$  to the porosity of the gas diffusion layer. Following up on this we can speculate now that both  $m$  and  $n$  relate to water management issues: a partially dehydrated electrolyte membrane leads to a decrease in conductivity, which can be represented by  $m$ , whereas an excess in liquid water leads to a reduction in porosity and hence to an early onset of mass transport limitations, which can be captured by the parameter  $n$ . Recently, Natarajan and Nguyen [27] have shown, how strongly the cell potential depends on the saturation level of the air. Note also that both these effects are not accounted for by the first two loss terms in Eq. (12).

Fig. 5 shows the effect of temperature on the fuel cell performance, as was measured by Kim et al. [25]. Note that in this case the stoichiometric flow ratio was only 1.5, which

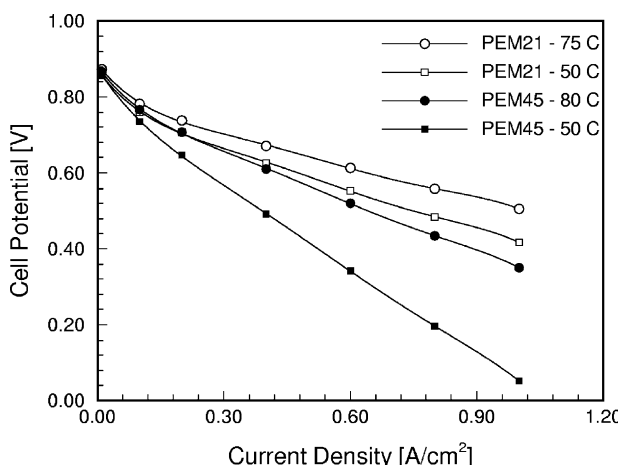


Fig. 4. Polarization curves for different temperatures obtained by Ticianelli et al.

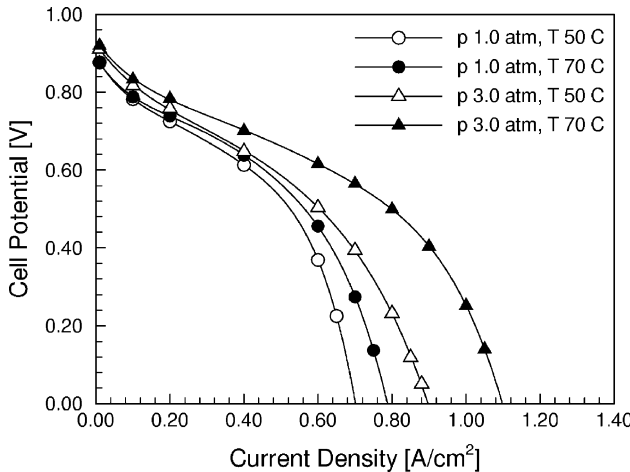


Fig. 5. Polarization curves for different temperatures and pressures reproduced from Kim et al.

led to relatively low limiting current densities. The importance of the stoichiometric flow ratio is discussed in detail in a later section. The qualitative agreement between the experimental data and numerical predictions is good, except for the high current density region. This is due to the fact that the calculated cell voltage in our model assumes a fully hydrated membrane at all times and a constant porosity of the gas diffusion layers, neglecting the onset of pore-plugging by liquid water.

### 3.2. Effect of pressure

Similar to the temperature, the operating pressure affects numerous parameter that are important for the fuel cell operation, among which are as follows.

- The *inlet gas compositions*. Because the saturation pressure of water vapour depends only on the temperature, a change in the operating pressure leads to a change in the inlet gas compositions, assuming the inlet gases are fully humidified.
- The *exchange current density*  $i_0$  of the oxygen reduction reaction. The dependence of the cathodic exchange current density on the oxygen pressure was also investigated experimentally by Parthasarathy et al. [28].
- The *reference potential*  $E_r$ . According to the Nernst equation, an increased pressure leads to an increase in the equilibrium potential.
- The *gas-pair diffusivities*  $D_{ij}$  in the Stefan–Maxwell equations. It is well known that the product of pressure and the binary diffusivity is constant [19]. Hence, a doubling of the pressure will cut the binary diffusivity in half.

Since the saturation pressure for water is only a function of temperature, it remains constant for a variation of the inlet pressure, and the molar fraction of water vapour in the incoming cathode gas stream is given by Eqs. (6) and (7). The molar oxygen fraction results then out of Eq. (8).

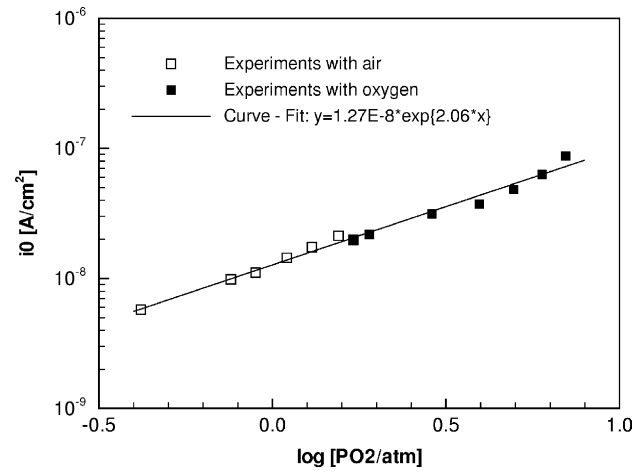


Fig. 6. The dependence of the exchange current density of the oxygen reduction reaction on the oxygen pressure.

It was already noted in Fig. 2 that the change in the inlet gas composition is particularly strong in the range from 1 to 3 atm. Above 3 atm the composition changes only slightly with the pressure.

In order to understand the dependence of the exchange current density  $i_0$  on the partial oxygen pressure, Parthasarathy et al. [28] conducted experiments at a temperature of 50 °C. The results are summarized in Fig. 6.

A linear relationship was found between the logarithm of the exchange current density  $i_0$  and the logarithm of the oxygen partial pressure, according to:

$$i_0 = 1.27 \times 10^{-8} \exp(2.06 p_{O_2}) \quad (13)$$

Because the temperature was different from our case and the roughness factor or catalyst loading was not reported, the values obtained with Eq. (12) had to be further scaled using the base case value of  $i_0 = 4.4 \times 10^{-7} \text{ A/cm}^2$  as a reference value. The detailed procedure is outlined in [20].

Table 3 summarizes the exchange current density used for our simulations. The third column lists the exchange current density as was calculated using Eq. (12) and the partial oxygen pressure as listed in the second column, and the last column contains the scaled values for the different temperature and catalyst loading. It can be seen that the pressure has a much weaker effect on the exchange current density than the temperature.

Although it is known that the reference exchange potential at the cathode side is a mixed potential due to competing

Table 3  
Exchange current density of the ORR as a function of pressure

$p$ (atm)	$p_{O_2}$ (atm)	$i_0$	
		$T = 50^\circ\text{C}$	$T = 80^\circ\text{C}$
1.0	0.1251	$1.64 \times 10^{-8}$	$0.78 \times 10^{-7}$
1.5	0.1483	$1.72 \times 10^{-8}$	$0.82 \times 10^{-7}$
3.0	0.5451	$3.90 \times 10^{-8}$	$1.85 \times 10^{-7}$
5.0	0.9650	$9.27 \times 10^{-8}$	$4.40 \times 10^{-7}$

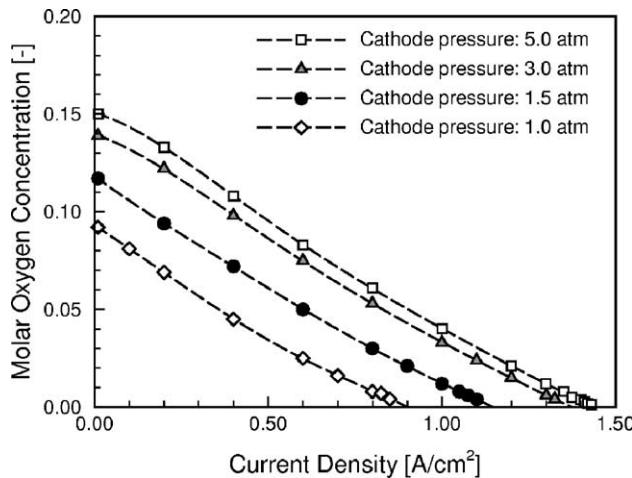


Fig. 7. Average molar oxygen fraction at the cathode side catalyst layer as function of the operating pressure.

reactions [28], the adjustment of the reference potential  $E$  was done according to the corrected Nernst equation in our case, and the diffusion coefficients for the Stefan–Maxwell equations were adjusted automatically in our model.

With the functional variations of the transport parameters determined, computations were performed for various operating pressures. Fig. 7 shows the average molar oxygen fraction at the cathode side catalyst layer, which eventually determines the limiting current density. The stoichiometric flow ratio is maintained constant at 3.0 in all these cases. The higher oxygen fraction at the cathode side inlet eventually leads to a higher maximum current. The increase is significant, when the pressure increases from atmospheric pressure to 3 atm, and this is consistent with Fig. 2. Further increase in pressure from 3.0 to 5.0 atm does not lead to a significant improvement in terms of the limiting current density. It should be emphasized again that this presumes the incoming gases are fully humidified.

The polarization curves shown in Fig. 8 reveal a significant change in the initial drop-off, when the pressure is

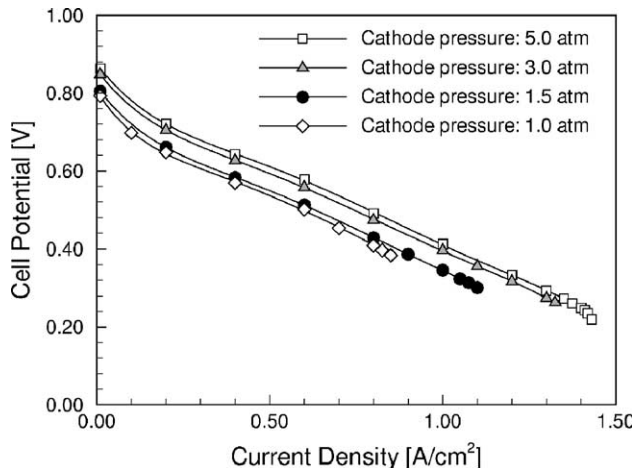


Fig. 8. Calculated polarization curves for various operating pressures.

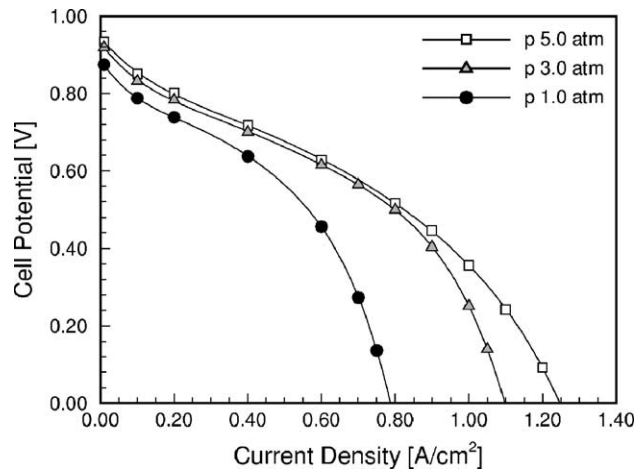


Fig. 9. Experimentally observed polarization curves for various cathode side pressures at a temperature of 70 °C and a stoichiometric flow ratio of 1.5.

changed. This can be attributed to the change in the equilibrium potential that goes along with a decrease in the reactant pressure (Nernst equation). To a much lesser extend, the decrease in the exchange current density with decreasing pressure also contributes to this effect.

Again, a detailed comparison with experimental results from the literature can only be made on a qualitative basis, since the exact conditions of the various experiments are not reported. In Fig. 9, experimentally obtained polarization curves by Kim et al. [25] are reproduced. The experiments were conducted with pure hydrogen at the anode side and air at the cathode side. Although the exact details of the experiments such as the cell geometry are not known, the two main effects that the cathode side pressure has on the fuel cell performance can be observed: the increase of the limiting current density with an increase in pressure and an overall better cell performance, which can be attributed to an increase in the equilibrium potential as well as reduced activation losses. It is interesting to note that the measured polarization curves for 3.0 and 5.0 atm are relatively close, which agrees well with the modelling results shown above.

In general it is difficult to compare the results obtained with the current model with experimental results taken from the literature, since various parameters that are not given in the literature influence the fuel cell performance. The gradual decrease in performance with current density that has been observed by Kim et al. [25] can currently not be captured with our model and we have reason to believe that it is associated with water management issues such as a partial dehydration of the membrane. Qualitative agreement, however, is very good and the principal physical benefits of operating a fuel cell at an elevated pressure have been confirmed.

### 3.3. Effect of stoichiometric flow ratio

The stoichiometric flow ratio is an important parameter, as it is the inverse of the fuel utilization and hence directly

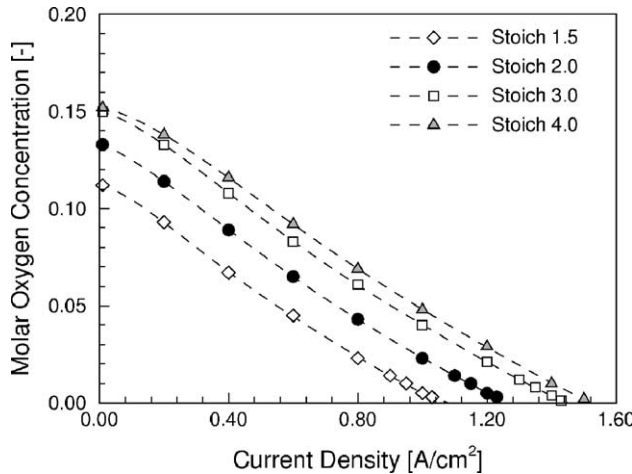


Fig. 10. Average molar oxygen fraction at the cathode side catalyst layer as function of current density for different values of the stoichiometric flow ratio.

affects the theoretical fuel cell efficiency [29]. In practice, the stoichiometric flow ratio has an impact on the limiting current density, but, more importantly, on water management issues [29], which can not be resolved with the current version of our model. The effect of the stoichiometric flow ratio on the limiting current density is shown in Fig. 10. The limiting current density is reached, when the oxygen concentration at the catalyst layer becomes zero. Because the stoichiometric flow ratio is constant even for extremely small current densities, the average molar oxygen fraction at

the catalyst layer approaches the inlet molar oxygen fraction of around 18% only for very high stoichiometric flow ratios (because the currents can be extremely small, stoichiometric flow ratios are often in the several hundreds in this region). Apart from that it can be observed that the lines are equidistant to one another and an increase in the stoichiometric flow ratio leads to an increase in the limiting current density region. However, beyond a value of 3.0 the gain in current density is relatively small, compared to the gain in the region below a value of 2.0. This graph also suggests that there is an inherent limitation to the attainable current density, as the slope does not change for a change in the stoichiometric flow ratio. We will see below that this slope depends on various parameters such as the GDE porosity and channel spacing.

A higher stoichiometric flow ratio also results in a more even distribution of the local current density, as is shown in Fig. 11. It was observed before that under the conditions investigated the amount of current generated under the channel area increases almost linearly with the current density, until the limiting current is reached [13]. This also leads to the fact that for a lower stoichiometric flow ratio at a constant current density, there is a much stronger distribution of current inside the cell, the maximum local current density being at the inlet under the channel area.

### 3.4. Effect of GDE porosity

The porosity of the gas diffusion layer has two competing effects on the fuel cell performance: as the porous region

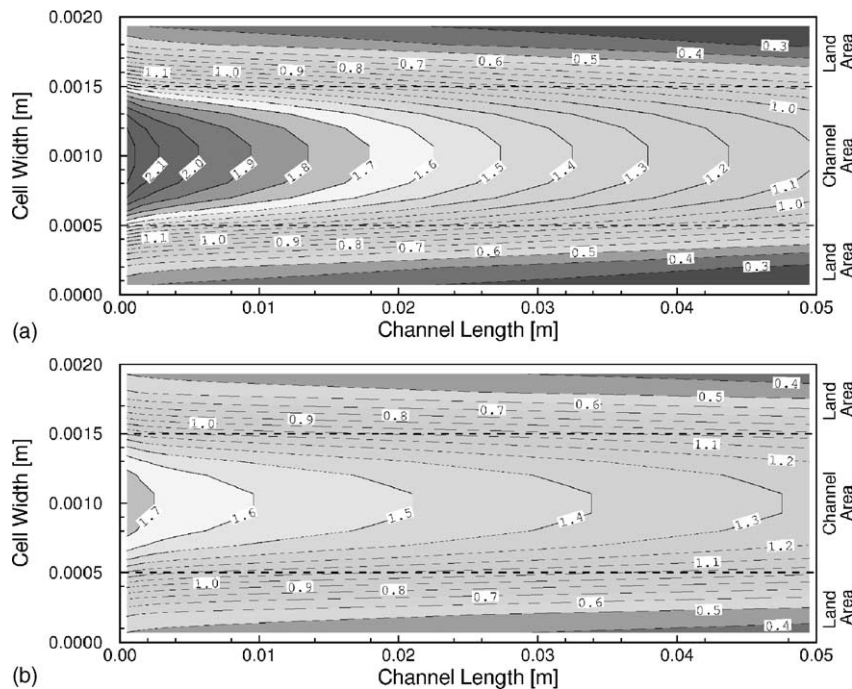


Fig. 11. Local current density distribution at the cathode side catalyst layer for a stoichiometric flow ratio of 2.0 (a) and 4.0 (b). The average current density is 1.0 A/cm<sup>2</sup>.

provides the space for the reactants to diffuse towards the catalyst region, an increase in the porosity means that the onset of mass transport limitations occurs at higher current densities, i.e. it leads to higher limiting currents. The adverse effect of a high porosity is an expected increase in the contact resistance. Contact resistance occurs at all interfaces inside the fuel cell, the most important one being the interface between the bipolar plates and the gas diffusion layers, and its magnitude depends on various parameters such as the surface material and treatment and the applied stack pressure. As the electrons travel through the solid matrix of the GDE, it can be assumed that the contact losses increase linearly with an increased porosity. The extend of contact losses has been measured by Barbir et al. [30], who found that for their “standard” fuel cell, the contact resistance can be as high as  $150 \text{ m}\Omega \text{ cm}$ , i.e. the voltage loss due to contact resistance at a current density of  $1.0 \text{ A}/\text{cm}^2$  would be as high as 0.15 V. In order to include the loss due to contact resistance in our model, we assumed a resistance at base case conditions ( $\varepsilon = 0.4$ ) and scaled this linearly with the porosity of the GDE.

Fig. 12 shows the average molar oxygen fraction at the cathode side catalyst layer as function of current density. It can be seen that the porosity has a significant effect on the limiting current density. An increase in the porosity of the GDE from  $\varepsilon = 0.3$  to 0.5 more than triples the value for the attainable current density from around  $0.75 \text{ A}/\text{cm}^2$  to just below  $2.4 \text{ A}/\text{cm}^2$ . This is because the transport inside the gas diffusion electrodes is primarily diffusive, and the binary

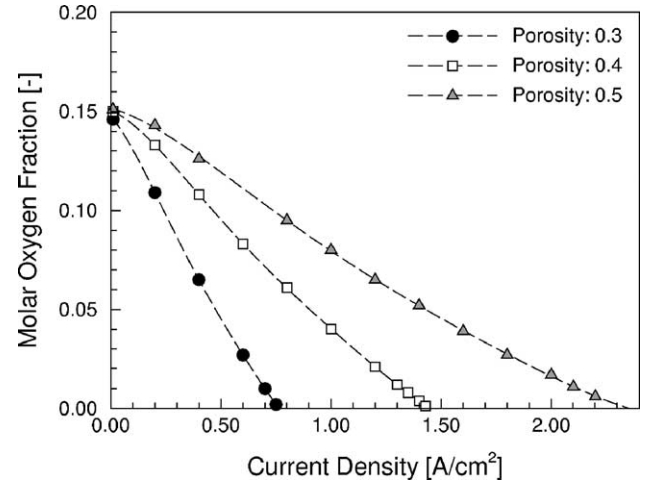


Fig. 12. Average molar oxygen fraction at the catalyst interface as function of current density for three different GDE porosities.

gas diffusivities are scaled by the so-called Bruggemann correction [1], where the porosity affects the diffusivity by a power of 1.5.

In addition, a higher porosity evens out the local current density distribution, as shown in Fig. 13. For a lower value of the porosity a much higher fraction of the total current is generated under the channel area. This can lead to local hot-spots inside the membrane, which can lead to a further drying out of the membrane, thus increasing the electric resistance, which in turn leads to more heat generation and

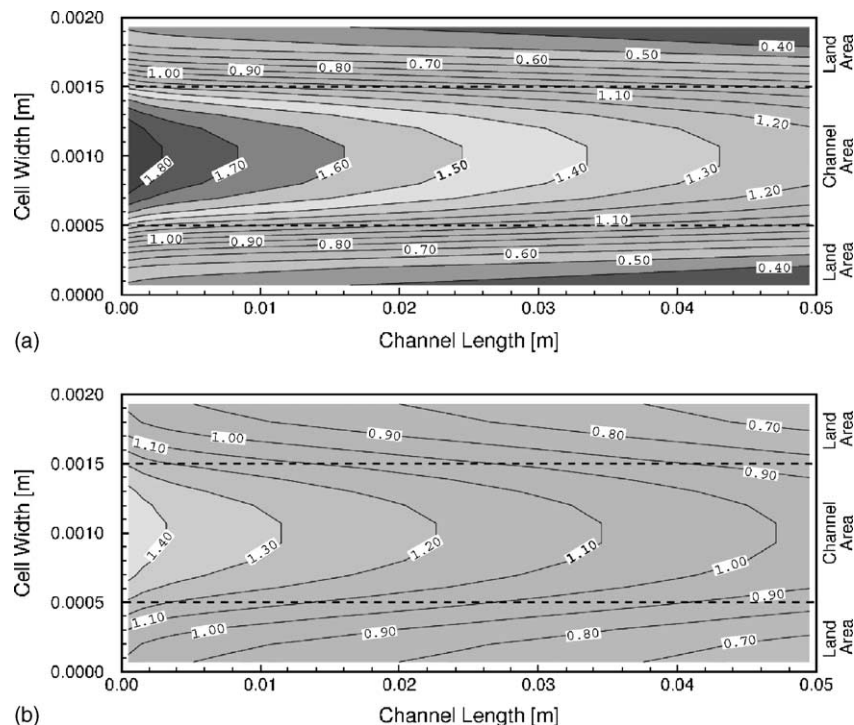


Fig. 13. Local current density distribution at the cathode side catalyst layer for a GDE porosity of 0.4 (a) and 0.6 (b). The average current density is  $1.0 \text{ A}/\text{cm}^2$ .

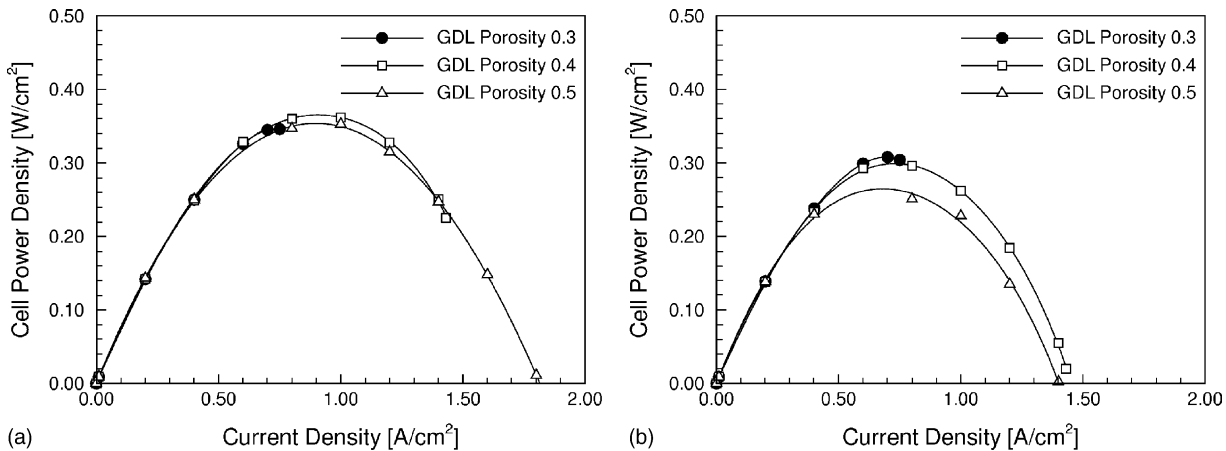


Fig. 14. Power density curves for three different GDE porosities and an assumed contact resistance at base case ( $\varepsilon = 0.4$ ) of  $50 \text{ m}\Omega \text{ cm}^2$  (a) and  $150 \text{ m}\Omega \text{ cm}^2$  (b).

can lead to a failure of the membrane. Thus, it is important to keep the current density relatively even throughout the cell.

Fig. 14 shows the calculated power density curves for different porosities and two assumed values for the contact resistance at base case conditions. It can be seen that for an assumed contact resistance of  $50 \text{ m}\Omega \text{ cm}^2$  all three power density curves remain fairly close.

As was seen before, the curve is cut off for a porosity of  $\varepsilon = 0.3$  because of the early onset of mass transport limitations. For a porosity of  $\varepsilon = 0.5$  the maximum attainable is not limited by the mass transport anymore, because this would occur only at a current density of  $2.4 \text{ A}/\text{cm}^2$ . The ohmic loss becomes so high that the cell voltage and hence the power density become zero at a current density of  $1.8 \text{ A}/\text{cm}^2$ . For a contact resistance of  $150 \text{ m}\Omega \text{ cm}^2$  the ohmic losses at the highly porous GDE become so high that the maximum power density is achieved by the cell with the lowest porosity. However, due to the early onset of mass transport limitations, a porosity of 0.4 appears to be the optimum under the current conditions.

### 3.5. Effect of the channel width

For the width of the fuel cell channel the same arguments hold as for the porosity, as the predominant parameters affected are the limiting current density in the form of mass transport limitations and on the other hand contact resistance. In addition, the pressure drop inside the cell will depend on the channel width. In our computations, we have left the overall pitch between channels constant, i.e. we changed the ratio between the channel width and the shoulder width, which in the base case is one, as both the channel and the land area are both 1 mm wide. Fig. 15 shows that the effect of the channel width on the limiting current density is not quite as strong as the effect of the porosity.

The local current density distribution for the cases with a channel and land area width of 0.8 mm/1.2 mm and 1.2 mm/0.8 mm, respectively, is shown in Fig. 16.

For the narrow channel the local current density can exceed more than twice the value as the average current density with a sharp drop-off under the land area, where the local current density is below  $0.2 \text{ A}/\text{cm}^2$ . The wider channel makes for a much more evenly distributed current throughout the cell.

The drawback of a wider channel is the reduction in contact area between the GDE and the bipolar plates, increasing the contact resistance. Fig. 17 shows the power density curves for two assumed values for the contact resistance at base case (Ch/L: 1 mm/1 mm). The advantage in terms of power density becomes pronounced at contact resistance of higher than  $50 \text{ m}\Omega \text{ cm}^2$ . For an assumed contact resistance of  $150 \text{ m}\Omega \text{ cm}^2$  at the base case, the limiting current density is the same for the cases with a 1 mm wide channel and a channel width of 1.2 mm, because at the widest channel the

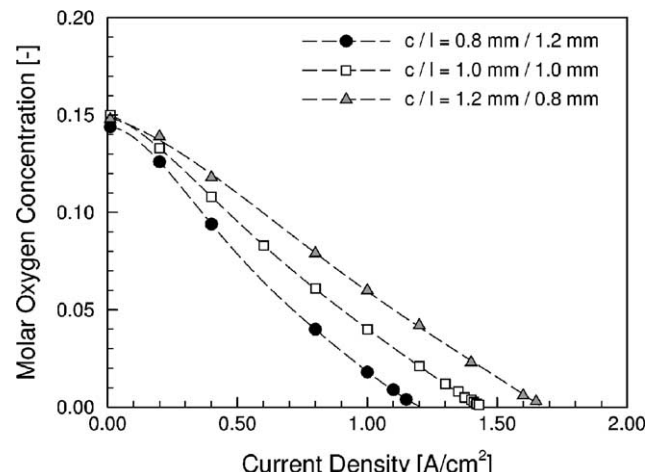


Fig. 15. Average molar oxygen fraction at the cathode side catalyst layer for three different values of the channel and land area width.

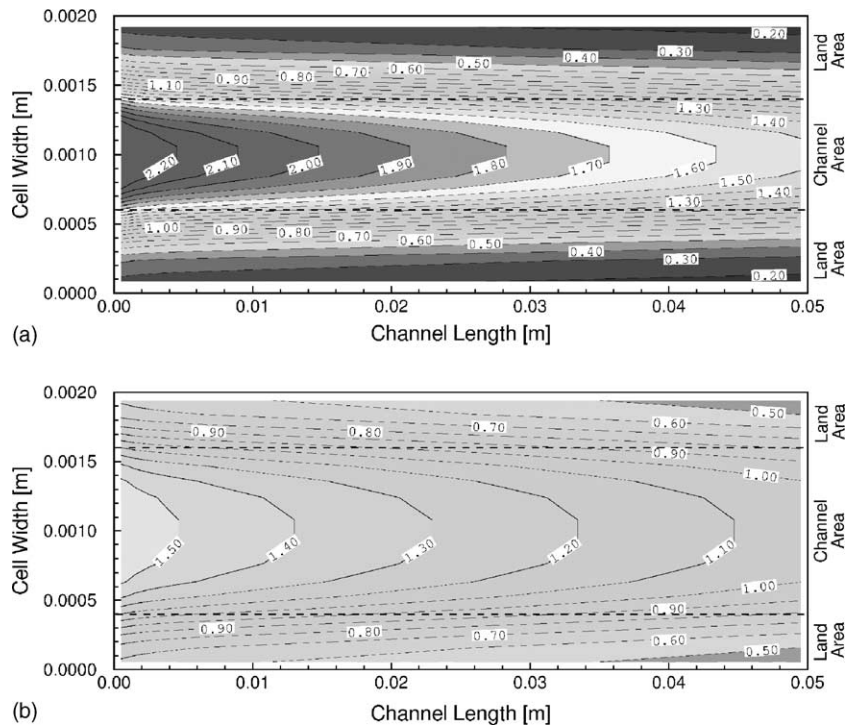


Fig. 16. Local current density distribution at the cathode side catalyst layer for a channel width of 0.8 mm (a) and 1.2 mm (b). The average current density is  $1.0 \text{ A}/\text{cm}^2$  in both cases.

limiting current density is again determined by the ohmic losses, not by mass transport limitations.

### 3.6. Effect of GDE thickness

The effect of the GDE thickness on the fuel cell performance is again mostly on the mass transport, as the ohmic losses of the electrons inside the GDE can be neglected due to the high conductivity of the carbon fiber paper. Fig. 18 shows the impact of the GDE thickness on the attainable current density. It is also interesting to note that at low cur-

rent densities an increased GDE thickness leads to a higher average oxygen fraction than for a thinner GDE. The reason for this is that a thicker GDE gives the oxygen more room to spread out in the lateral ( $z$ -) direction under the land area. The current density, where these lines cross, depends on the ratio between the channel width and the land area, and it is worth exploring, how strongly. The right hand side of Fig. 18 shows the same plot for a channel width of 0.8 mm and a land area width of 1.2 mm. In this case, the lines cross at a current density of  $0.4 \text{ A}/\text{cm}^2$ , which means that this effect is not of practical importance.

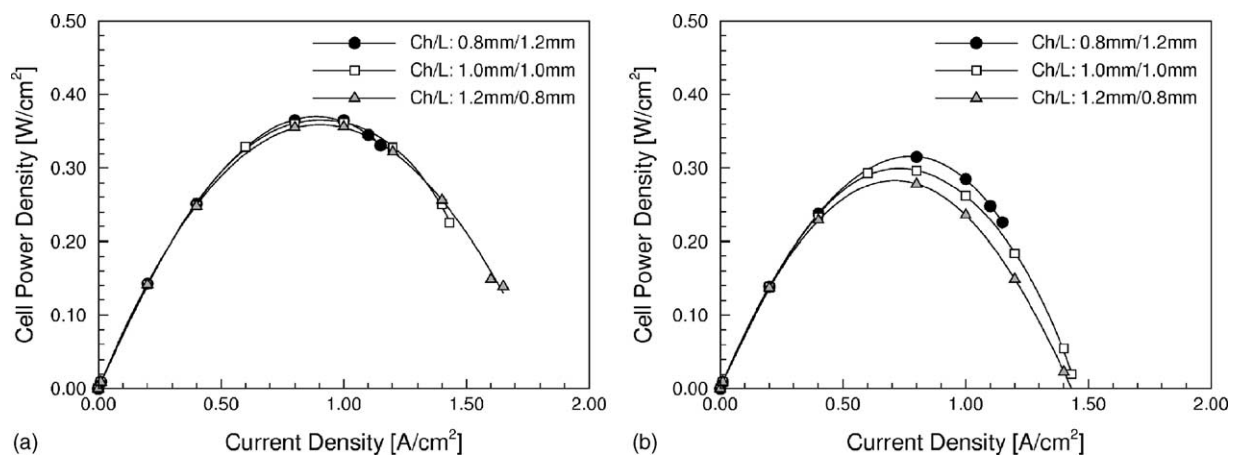


Fig. 17. Power density curves for different channel widths and two assumed values for the contact resistance at base case.

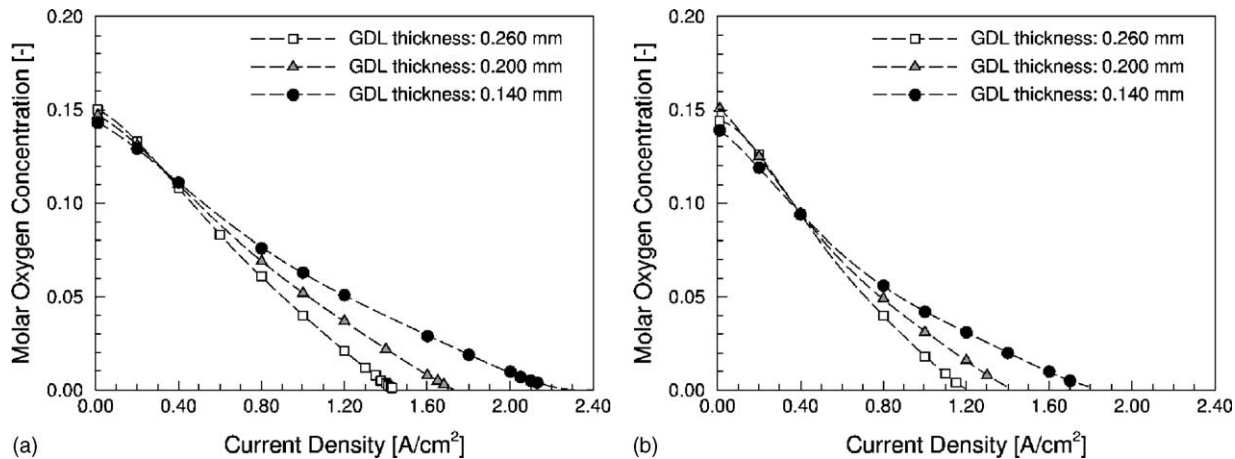


Fig. 18. Average molar oxygen fraction at the cathode side catalyst layer for different GDE thicknesses as function of current density. Part (a) is for a channel width of 1 mm and (b) for 0.8 mm.

#### 4. Conclusions

A parametric study using a three-dimensional model of a PEM fuel cell has been performed. The study quantifies the impact of operating and geometric parameters on performance. Experiments with respect to the effect of temperature and pressure are well documented in the literature, and the results obtained with our model reproduce all the trends and highlight the importance of properly accounting for the effect of operational parameters on transport and kinetic properties.

In addition, material properties such as the GDE thickness and porosity as well as the channel width compared to the land area have been investigated. It was found that the porosity of the gas diffusion layer has a strong effect on the limiting current density. In order to properly assess the impact of porosity and channel width on performance, it was necessary to estimate the extend of contact resistance inside the fuel cell.

Overall, this study demonstrates the use of a comprehensive three-dimensional single-phase model as a design tool. Further capability enhancement requires the modelling of two-phase transport and phase change in the gas diffusion electrodes. Work is in progress that addresses these issues.

#### Acknowledgements

The authors would like to thank Dr. Dongming Lu for his contributions to the initial model development.

#### References

- [1] D.M. Bernardi, M.W. Verbrugge, Mathematical model of a gas diffusion electrode bonded to a polymer electrolyte, *Am. Inst. Chem. Eng. J.* 37 (8) (1991) 1151–1163.
- [2] D.M. Bernardi, M.W. Verbrugge, A mathematical model of the solid-polymer-electrode fuel cell, *J. Electrochem. Soc.* 139 (9) (1992) 2477–2491.
- [3] T.E. Springer, T.A. Zawodzinski, S. Gottesfeld, Polymer electrolyte fuel cell model, *J. Electrochem. Soc.* 138 (8) (1991) 2334–2342.
- [4] T.F. Fuller, J. Newman, Water and thermal management in solid-polymer-electrolyte fuel cells, *J. Electrochem. Soc.* 140 (5) (1993) 1218–1225.
- [5] T.V. Nguyen, R.E. White, A water and heat management model for proton-exchange-membrane fuel cells, *J. Electrochem. Soc.* 140 (8) (1993) 2178–2186.
- [6] J.S. Yi, T.V. Nguyen, An along-the channel model for proton exchange membrane fuel cells, *J. Electrochem. Soc.* 145 (4) (1998) 1149–1159.
- [7] M. Wöhr, K. Bolwin, W. Schnurnberger, M. Fischer, W. Neubrand, G. Eigenberger, Dynamic modelling and simulation of a polymer membrane fuel cell including mass transport limitations, *Int. J. Hydrogen Energy* 23 (3) (1998) 213–218.
- [8] N. Djilali, D.M. Lu, Influence of heat and mass transfer on gas and water transport in fuel cells, *Int. J. Therm. Sci.* 41 (2002) 29–40.
- [9] J.J. Baschuk, X. Li, Modelling of polymer electrolyte membrane fuel cells with variable degrees of water flooding, *J. Power Sources* 86 (2000) 181–195.
- [10] V. Gurau, H. Liu, S. Kakac, Two-dimensional model for proton exchange membrane fuel cells, *Am. Inst. Chem. Eng. J.* 44 (11) (1998) 2410–2422.
- [11] Z.H. Wang, C.Y. Wang, K.S. Chen, Two-phase flow and transport in air cathode of proton exchange membrane fuel cells, *J. Power Sources* 94 (2001) 40–50.
- [12] S. Um, C.Y. Wang, K.S. Chen, Computational fluid dynamics modeling of proton exchange membrane fuel cells, *J. Electrochem. Soc.* 147 (12) (2000) 4485–4493.
- [13] T. Berning, D. Lu, N. Djilali, Three-dimensional computational analysis of transport phenomena in a PEM fuel cell, *J. Power Sources* 106 (2002).
- [14] S. Dutta, S. Shimpalee, J.W. Van Zee, Three-dimensional numerical simulation of straight channel PEM fuel cells, *J. Appl. Electrochem.* 30 (2000) 135–146.
- [15] R. Taylor, R. Krishna, *Multicomponent Mass Transfer*, Wiley, New York, 1993.
- [16] A.J. Bard, L.R. Faulkner, *Electrochemical Methods*, Wiley, New York, 1980.
- [17] R. Schlögl, Membrane permeation in systems far from equilibrium, *Ber. Bunsenges. Phys. Chem.* 70 (4) (1966) 400–414.

- [18] A. Parthasarathy, S. Srinivasan, J.A. Appleby, C.R. Martin, Temperature dependence of the electrode kinetics of oxygen reduction at the platinum/Nafion interface: a microelectrode investigation, *J. Electrochem. Soc.* 139 (9) (1992) 2530–2537.
- [19] E.L. Cussler, *Diffusion: Mass Transport in Fluid Systems*, Cambridge University Press, Cambridge, 1984.
- [20] T. Berning, *Three-Dimensional Computational Analysis of Transport Phenomena in a PEM Fuel Cell*, PhD Thesis, University of Victoria, Victoria, 2002.
- [21] R.B. Bird, W. Steward, E.N. Lightfoot, *Transport Phenomena*, Wiley, New York, 1960.
- [22] M.W. Verbrugge, R.F. Hill, Transport phenomena in perfluorosulfonic acid membranes during the passage of current, *J. Electrochem. Soc.* 137 (4) (1990) 1131–1138.
- [23] J. O'M. Bockris, S. Srinivasan, *Fuel Cells: Their Electrochemistry*, McGraw-Hill, New York, 1969.
- [24] E.A. Ticianelli, C.R. Derouin, A. Redondo, S. Srinivasan, Methods to advance technology of proton exchange membrane fuel cells, *J. Electrochem. Soc.* 135 (9) (1988) 2209–2214.
- [25] J. Kim, S.-M. Lee, S. Srinivasan, C.E. Chamberlin, Modelling of proton exchange membrane fuel cell performance with an empirical equation, *J. Electrochem. Soc.* 142 (8) (1995) 2670–2674.
- [26] D. Bevers, M. Wöhr, K. Yasuda, K. Oguro, Simulation of a polymer electrolyte fuel cell electrode, *J. Appl. Electrochem.* 27 (1997) 1254–1264.
- [27] D. Natarajan, T.V. Nguyen, A two-dimensional, two-phase, multi-component, transient model for the cathode of a proton exchange membrane fuel cell using conventional gas distributors, *J. Electrochem. Soc.* 148 (12) (2001) A1324–A1335.
- [28] A. Parthasarathy, S. Srinivasan, J.A. Appleby, C.R. Martin, Pressure dependence of the oxygen reduction reaction at the platinum micro-electrode/Nafion interface: electrode kinetics and mass transport, *J. Electrochem. Soc.* 139 (10) (1992) 2856–2862.
- [29] J. Larminie, A. Dicks, *Fuel Cells Systems Explained*, Wiley, Chichester, 2000.
- [30] F. Barbir, J. Braun, J. Neutzler, Properties of molded graphite bi-polar plates for PEM fuel cell stacks, *J. New Mater. Electrochem. Syst.* 2 (1999) 197–200.